nature nanotechnology

SUPPLEMENTARY INFORMATION

DOI: 10.1038/NNANO.2014.175

Manipulation of the nuclear spin ensemble in a quantum dot with chirped magnetic resonance pulses

Mathieu Munsch, Gunter Wüst, Andreas V. Kuhlmann, Fei Xue, Arne Ludwig,

Dirk Reuter, Andreas D. Wieck, Martino Poggio, and Richard J. Warburton

(Dated: June 30, 2014)

CONTENTS

I. EXPERIMENTAL DETAILS

A. Sample

Our sample consists of low density self-assembled InGaAs/GaAs quantum dots (QDs) grown by molecular beam epitaxy embedded in the intrinsic region of an n-type GaAs Schottky diode (see Fig. S1). The layers in the heterostructure are:

I. Back gate: 50 nm Si-GaAs, doping $n = 1.7 \times 10^{18}\,\mathrm{cm}^{-3}$

II. Tunnel barrier: 25 nm i-GaAs

III. Active region: InGaAs QDs

IV. Capping layer: 434.3 nm i-GaAs

V. Blocking barrier: 64 periods of 3 nm/1 nm AlAs/GaAs

VI. Top cap: 10 nm i-GaAs

VII. Top gate: 3 nm/7 nm Ti/Au

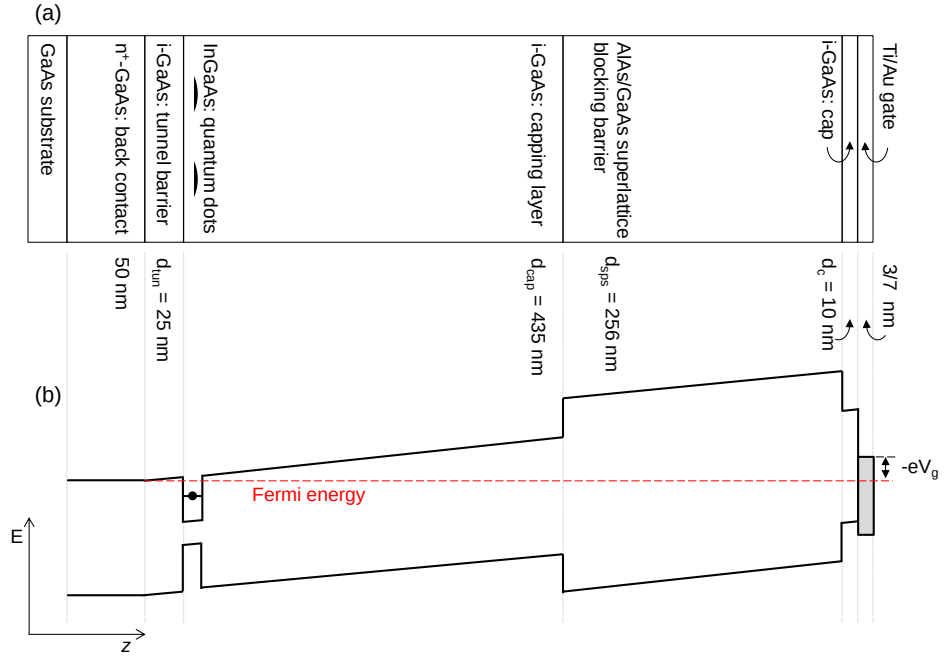

FIG. S1. **Sample structure**. (a) Layer structure of our sample. (b) Associated band structure. Applying a voltage V_g between top gate and back gate allows the QD energy levels to be tuned relative to the Fermi energy, which is determined by the n^+-doping of the back gate. Here the ground state of the X^{1-} is shown. The lever arm (distance between top and back gate divided by the thickness of the tunnel barrier) is 28.6.

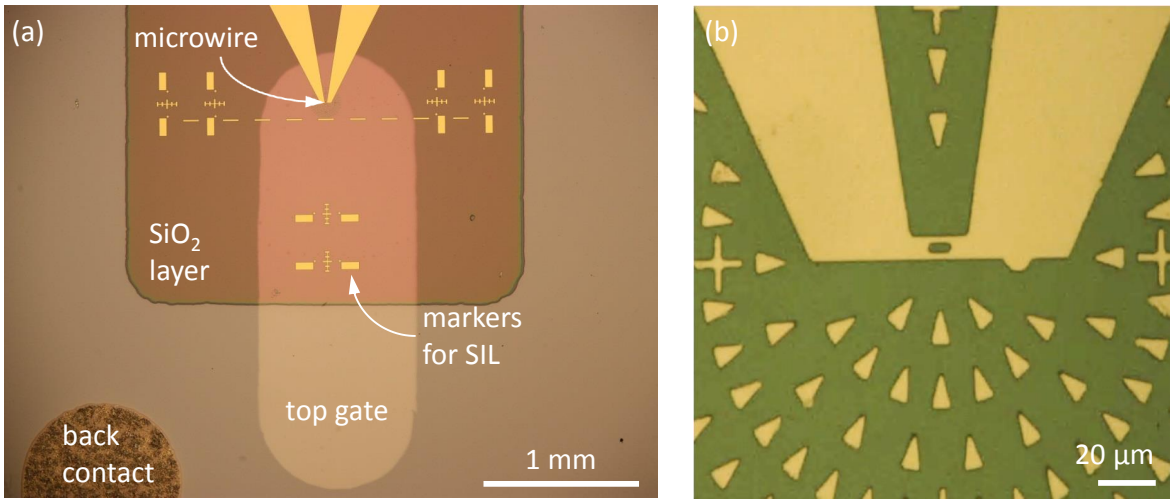

FIG. S2. **Top view of sample.** (a) Shadow masks are used to deposit back contact, top gate and SiO_2 spacer layer. Microwire and markers for positioning the solid immersion lens are fabricated in one photolithography step. We minimize the overlap of the microwire and the top gate to reduce the risk of electrical shorts. Reducing the area of the SiO_2 layer circumvents adhesion problems. (b) Zoom in on the microwire. A hole in the wire enables optical access to the QD emission. Triangular markers facilitate the positioning of the sample in the microscope.

To generate the longitudinal radio frequency (RF) field we fabricate a gold microwire directly on the sample. With a shadow mask we first deposit a 464 nm ($= \frac{3}{4}\lambda$, $\lambda = 950$ nm) thick SiO_2 spacer onto the top gate, which serves as an electrical and thermal insulator and as an anti-reflection coating. We then deposit a 10/200 nm Ti/Au microwire with a photolithography procedure. The wire is 20 µm long, 6 µm wide and has a 2 µm by 6 µm hole, through which QD emission is detected (Fig. S2). On top of the structure, a ZrO_2 solid immersion lens (SIL) (refractive index 2.15) is used to increase the detection efficiency by a factor of ~ 5. Markers fabricated together with the microwire allow the SIL to be centred precisely. To contact the back gate we deposit 120 nm AuGe and 10 nm Ni and anneal the sample at 450 °C.

B. Set-up

The sample is cooled down to 4.2 K in a helium bath cryostat (see Fig. S3). A superconducting magnet provides a static field B_z up to 9 T along the growth direction (Faraday geometry).

Initialization and read-out of the nuclear spin polarization is performed optically. We use resonant excitation of the X^0 transition which leads to the creation of a single electron-hole pair with no excess carriers. The resonance fluorescence is detected with a confocal dark-field microscope [1]. At $B_z = 0$ T, the ultra-high quality of the sample is revealed by the small measured linewidth of 1.2 µeV, close to the ideal transform limit of ~ 0.9 µeV (see Fig. 2 of main paper). At $B_z = 6$ T sweeping the laser energy across the

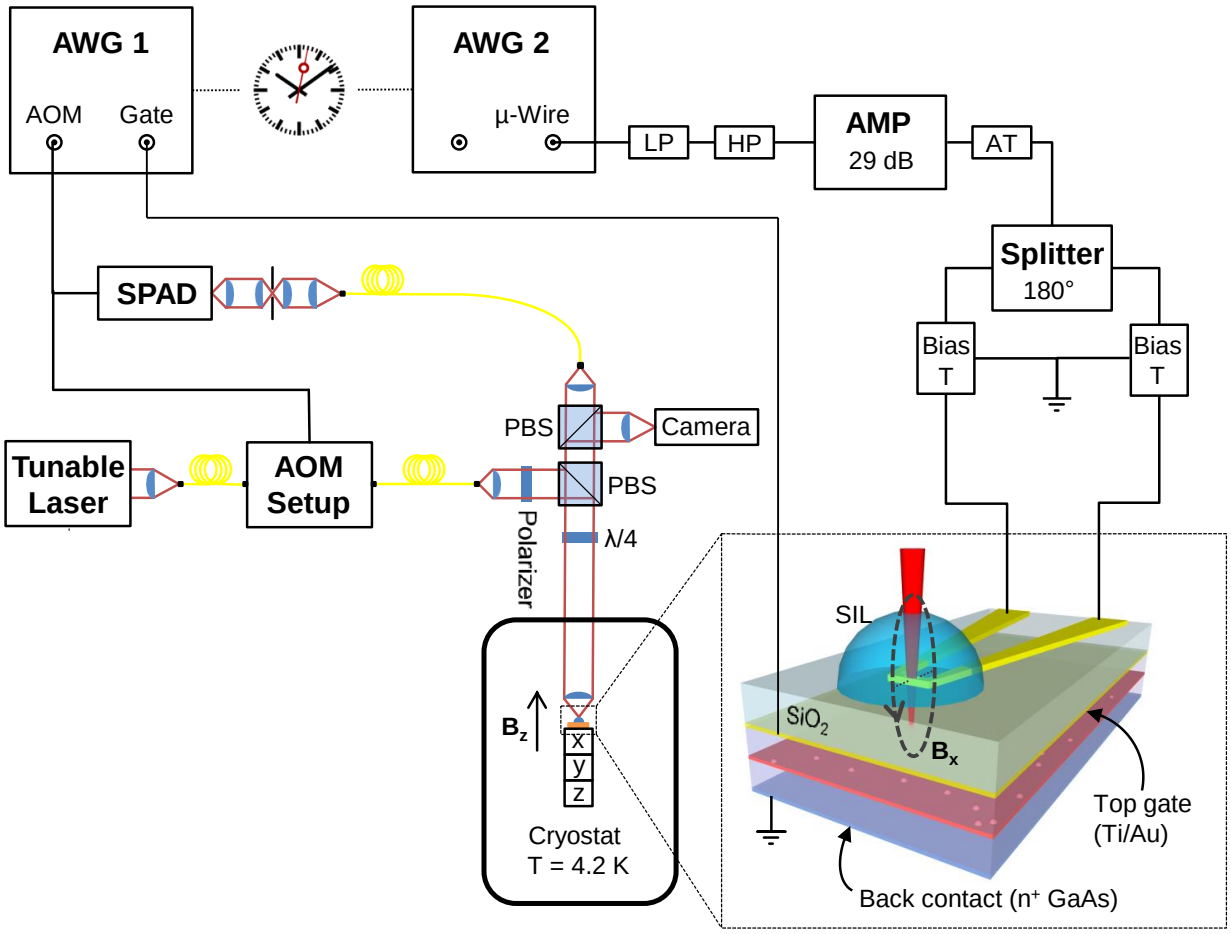

FIG. S3. **Experimental set-up.** The sample is mounted on a stack of X/Y/Z-piezo positioners and held at T = 4.2 K. Polarizing beam splitters (PBS), a polarizer and a quarter wave plate ($\lambda/4$) within the resonance fluorescence head enable high quality cross polarization between detection and excitation. A spatial filter in front of the single photon avalanche diode ensures a low dark count rate of ~ 10 counts/s. AWG 1 controls the laser intensity (via an AOM setup) and the laser detuning by sweeping the gate voltage. AWG 2 generates the the chirped RF pulses which are then sent to a current amplifier (AMP). High pass (HP) and low pass (LP) filters eliminate any unwanted noise and attenuators (AT) are used to adjust the amplitude. The signal is then sent through a splitter which induces a 180 ° phase shift between the different arms, thereby minimizing the electric field at the wire.

blue Zeeman transition of the X^0 leads to dynamical nuclear spin polarization via the so called "dragging effect" [2, 3]. The result is a characteristic flat-top spectrum. In practice, the detuning is achieved by sweeping the voltage applied to the gate, V_g. For the X^0, the Stark shift amounts to 0.447 ± 0.002 μeV/mV.

Two arbitrary waveform generators (AWGs) control and synchronize the experiment. The first one controls the voltage applied to the gate, as well as the laser intensity via an acousto-optic modulator (AOM) double passage set-up. The second one generates chirped pulses at radio frequencies. Its 512 MB internal memory allows for a maximum pulse duration of 1.3 s at a maximum sampling rate of 200 MHz. The

output voltage is sent to a RF amplifier and corrected for the frequency dependent gain of the amplifier. High pass (HP) filters at 25 MHz and low pass filters (LP) at 150 MHz eliminate possible noise. The signal is then split into two co-axial cables of the same length which go down into the cryostat. The last ~ 5 cm of the connection is made by a twisted pair. In one arm, the phase of the signal is shifted by π to avoid electric fields at the microwire which could influence the QD signal via the Stark effect. The DC-resistance measured at the top of the cryostat is R = 3.5 Ω. The amplitude of the output voltage at the top of the cryostat is measured over a 50 Ω resistance and kept at $V_{\mu wire} = 10$ V for all data presented in this work.

We sometimes observe random "rigid" shifts in the QD spectrum. For high voltages ($V_{\mu wire} \geq 12$ V) these shifts become disruptively large (up to 100 μeV to both higher or lower energy). We attribute these rigid shifts to a reorganisation of the defect charges in the vicinity of the QD. Importantly, our read-out technique allows us to distinguish between the these rigid shifts and the nuclear spin effects. In particular, the Overhauser shift is measured by the width of the dragging plateau which does not depend on the absolute frequency of the QD resonance. The data in Fig. 2 are corrected from these rigid shifts.

II. SUPPORTING EXPERIMENTAL RESULTS

A. Depolarization procedure

In order to randomize the QD spin ensemble, we use a series of short pulses whose frequencies cover the whole 55 MHz bandwidth spanned by the QD nuclei at $B_z = 6$ T. After a few minutes, the system reaches a stationary state, which corresponds to complete depolarization of the sample. This is reported in Fig. S4, where we plot the dragging plateau width as a function of the number of cycles. Before each measurement the system is initialized by dragging the QD transition from the blue, as described in the main article. The pulse duration is set to $4\,\mu$s, with a repetition rate of 25 kHz.

B. Nuclear-spin lifetime

A measurement of the nuclear spin relaxation in the lab frame shows that, after 22 hours, less than 30% of the initial polarization has relaxed (Fig. S5). The T_1 time of the nuclear spin ensemble clearly exceeds one day (we note that the decay is not a simple exponential). This extremely long decay time arises as a consequence of the suppression of nuclear spin diffusion into the bulk due to the strained environment of the QD [4] and the low temperature. Hence we can neglect relaxation on the time scale of our experiments.

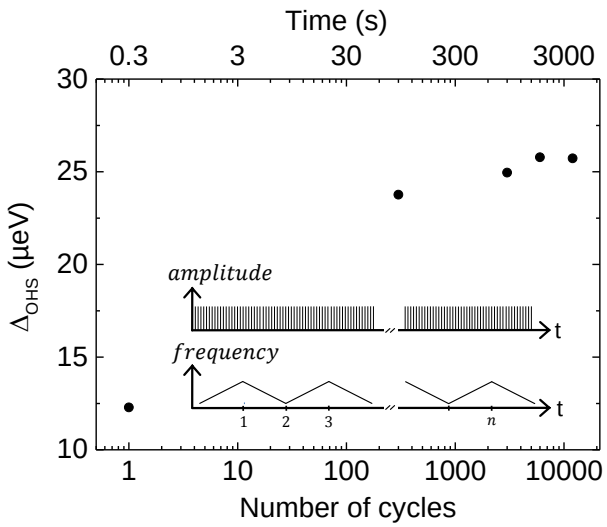

FIG. S4. **Randomization of the QD nuclear spin ensemble**. The randomization signal is obtained with current pulses in the wire at 25 kHz, with a duty cycle of 10% (see inset). The frequency is swept over 55 MHz to cover the complete bandwidth spanned by the QD nuclear spins. After ~ 600 s the system reaches a stationary state.

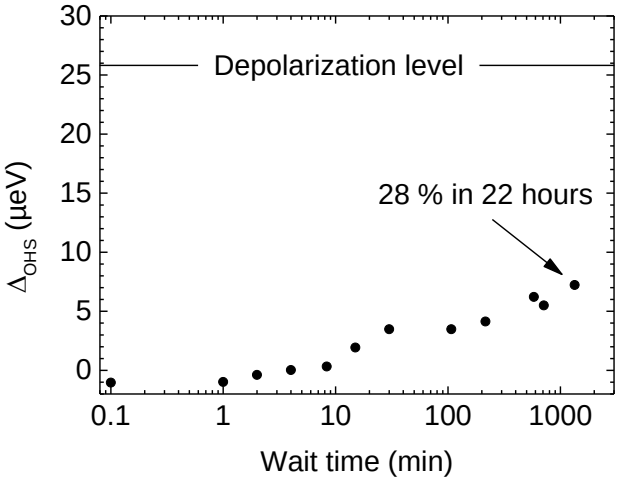

FIG. S5. **Nuclear spin relaxation in the laboratory frame.** The change in Overhauser shift following the decay of nuclear spin polarization is extremely slow and can be neglected on the few minute time scale of our experiments.

C. Measurement of Rabi oscillations and estimate of B_x

In order to estimate the magnitude of the radio frequency (RF) transverse magnetic field B_x produced by the microwire used in our optical experiments, we performed nutation measurements using a similar microwire in a magnetic resonance force microscope (MRFM). Using the method described in Poggio *et al.* [5], we measure the transverse field experienced by an ensemble of $\sim 10^{6}$ ^{115}In spins 350 nm from the microwire. These spins are contained within an InP nanowire in a 6 T magnetic field at a temperature of

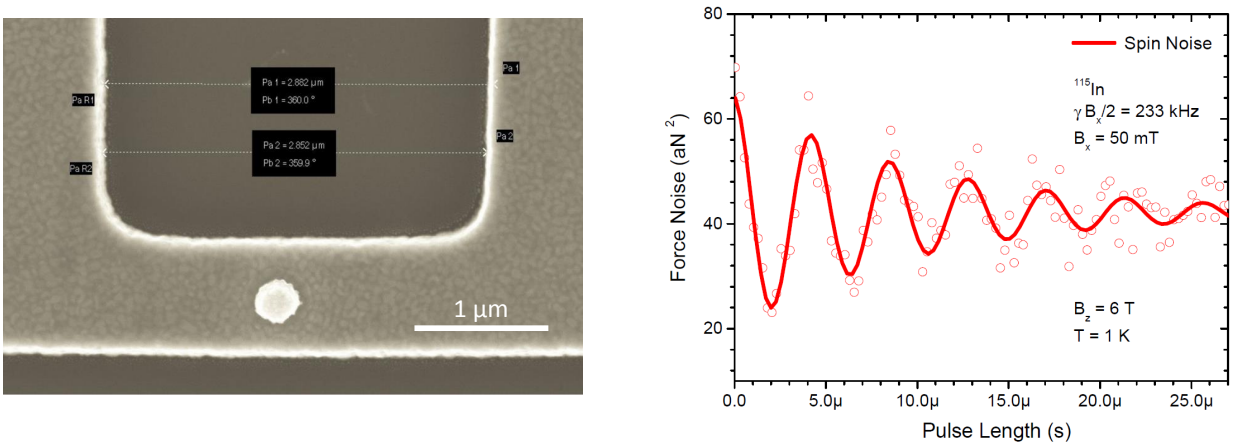

FIG. S6. **Nutation measurement for ^{115}In at T = 1 K.** (a) SEM micrograph of the 260 nm thick Au microwire with integrated FeCo tip used in the MRFM measurements. The microwire is 900 nm wide and 2.87 µm long. The structure is patterned on a Si chip. (b) Resonant force noise from ^{115}In spins (points) is measured as a function of pulse length according to the protocol described in [5]. A frequency of 233 kHz is obtained from a decaying sinusoidal fit (solid line) to the Rabi oscillations, resulting in $B_x = 50$ mT.

1 K. The experiment is carried out with an adiabatic rapid passage pulse protocol similar to the one used in the optical experiment at a carrier frequency of 57.25 MHz. To contact the microwire similar lengths of exactly the same type of coaxial lines and twisted pairs are used. Identical hardware is used to generate, split and filter the chirped pulses.

As shown in Fig. S6, the microwire in the MRFM generates 50 mT of transverse magnetic field (25 mT in the rotating frame). The amplitude of the drive voltage measured across 50 Ω at the same point at the top of the cryostat for the MRFM and the optical experiments is 8.5 $V_{p\text{-}to\text{-}p}$ and 10 $V_{p\text{-}to\text{-}p}$, respectively. Also, the geometry of the microwire in the MRFM differs from that used in the optical experiment, as shown in Fig. S6. Finally, the spin ensemble in the MRFM is located 350 nm above the microwire, while the QD in the optical experiment lies 1.17 µm below the microwire. By taking these differences into account, we use the magnitude of the transverse field measured by MRFM to estimate the field produced at the QD location in the optical experiment. In particular, these differences result in different currents passing through the two microwires and in different distances between the detection volume and the respective RF current. By approximating the two microwires as infinite wires, which produce a field decreasing inversely with the distance, we calculate the transverse field at the QD positon. For a drive of 10$V_{p\text{-}to\text{-}p}$ across 50 Ω, the QD microwire should generate $B_x = 5$ mT. The value $B_x = 3.8$ mT extracted from fits to our data is close to this estimation.

III. THEORY

A. Concepts

A1. Hamiltonian of a single spin I

During the manipulation step of our experiment, the evolution of a spin I can be described by the time-dependent Hamiltonian

$$H(t) = H_Z + H_Q + H_{RF}(t). \tag{1}$$

H_Z is the Zeeman energy, H_Q describes the interactions between the nuclear quadrupole moment and the electric field gradient (EFG) for a spin $I > \frac{1}{2}$ in a non-cubic lattice, and $H_{RF}(t)$ corresponds to the coupling to the transverse radio-frequency field. This is most conveniently expressed in the frame rotating at the Larmor frequency $\nu_L = \gamma B_z$, where γ is the gyromagnetic ratio of the nuclei and B_z the magnetic field applied along the z-direction (here the quantization axis). Using the rotating wave approximation to neglect fast oscillating terms [6] and assuming cylindrical symmetry of the EFG, $H(t)$ reduces to

$$H^{(1)}(t) = h\Delta\nu(t)I_z + \frac{h\nu_Q}{6}\left[3I_z^2 - I(I+1)\right] + \frac{h\nu_{RF}}{2}I_x \tag{2}$$

where $\Delta\nu(t)$ is the time-dependent detuning between the radio frequency and the Larmor frequency, $\nu_{RF} = \gamma B_x$ the amplitude of the RF field and ν_Q the quadrupole frequency. ν_Q describes the strength of the quadrupole interaction and depends on the nuclear quadrupole moment Q and on the EFG $V_{z'z'}$ along the symmetry axis z'. Writing θ as the angle between z and z', we find

$$\nu_Q = \frac{3eQV_{z'z'}}{4hI(2I-1)}[3\cos^2\theta - 1]. \tag{3}$$

We are interested in the eigenvalues of the problem for $I > \frac{1}{2}$. As an example, Fig. S7 shows the energy eigenstates for a spin $I = \frac{3}{2}$ as a function of the detuning $\Delta\nu(t)$. Six different transitions can be observed: three first-quantum transitions (QTs), often referred to as the central peak and its two satellites, two second-QTs and one third-QT, corresonding to a change in angular momentum of $|\Delta m| = 1, 2$ and 3, respectively. We note that each transition is well isolated, a consequence of $\nu_Q \gg \nu_{RF}$. A clear hierarchy of avoided crossings can be observed: the lower the order of the QT, the more pronounced the splitting. This result can be derived analytically in the limit where $\nu_Q \gg \nu_{RF}$ using an effective pseudo-spin 1/2 approach [7, 8], which yields the following expression for the coupling strengths

$$\nu_{\text{eff}}(\Delta m) = k(m_i, m_j)\nu_{RF}\left(\frac{\nu_{RF}}{\nu_Q}\right)^{|\Delta m|-1} \tag{4}$$

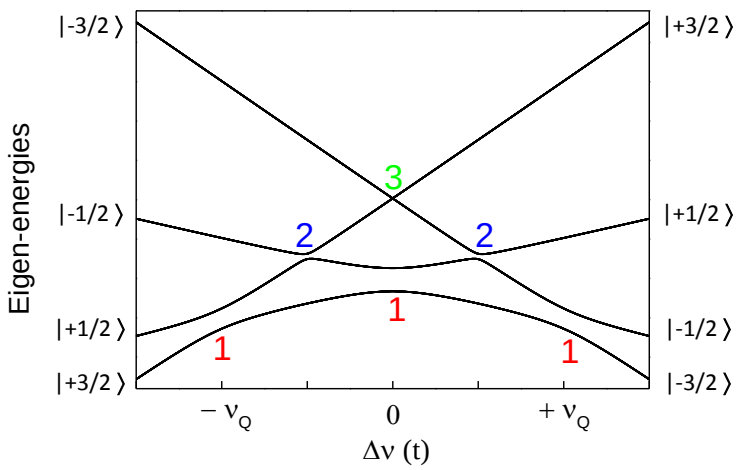

FIG. S7. **Energy level diagram for a spin $I = \frac{3}{2}$ in the rotating frame**. The calculation is carried out with $\frac{\nu_{RF}}{\nu_Q} = 0.15$. The eigenstates are labelled with the diabatic quantum number m in the limit of large detunings. The numbers in colour represent the order Δm associated with each transition.

where $k(m_i, m_j)$ is a scaling factor associated with the $|m_i\rangle \rightarrow |m_j\rangle$ transition. As an example we show, in Table I, the scaling factors associated with the $\frac{3}{2}$-spin. Since $\nu_Q \gg \nu_{RF}$ it is clear from Eq. 4 that $\nu_{\text{eff}}(\Delta m = 1) \gg \nu_{\text{eff}}(\Delta m = 2) \gg \nu_{\text{eff}}(\Delta m = 3)$. Remarkably, $\nu_{\text{eff}}(\Delta m = 1)$ does *not* depend on the quadrupole frequency to first order.

m_i / m_j	$3/2$	$1/2$	$-1/2$	$-3/2$
$3/2$	–	$\sqrt{3}$	$\frac{7}{2}$	$\frac{3}{2}$
$1/2$	$\sqrt{3}$	–	2	$\frac{7}{2}$

TABLE I. **Effective RF field scaling factors $k(m_i, m_j)$ for the first and multiple-quantum transitions of $I = \frac{3}{2}$ [8].**

A2. Adiabaticity criteria for a quadrupolar nucleus

To quantify the degree of adiabaticity of the manipulation, we assign a probability to each type of transition according to the Landau-Zener model (see Eq. 2 of the main paper)

$$P_{LZ}(\Delta m) = \exp\left(-\pi^2 \frac{\nu_{\text{eff}}^2(\Delta m)}{\alpha \Delta m}\right). \tag{5}$$

Note that, for higher-order transitions, the sweep rate α is replaced by an effective sweep rate $\alpha\Delta m$, which accounts for the magnified detuning rate (steepness of the level crossings in Fig. S7) [9]. P_{LZ} corresponds

to the probability that the system "tunnels" through the avoided crossing and stays on the same *diabatic* state. The condition for adiabatic passage is thus $P_{LZ} \ll 1$, which translates into low α and/or large ν_{eff}. Generally speaking, from Eqs. 4 and 5 it is clear that nuclei experiencing large quadrupole interactions are harder to manipulate. However, to first order, adiabatic passage is independent of the quadrupole interaction if it is possible to prepare the spins in their ground state, since the first QTs do not depend on ν_Q (see also end of the section).

In order to study the dynamics of the Landau-Zener problem in more detail we solve numerically the time-dependent von Neumann equation. Neglecting dissipation operators, the time-evolution of the density matrix $\rho(t)$ obeys

$$i\hbar\dot{\rho}(t) = [H(t),\rho(t)]\,. \tag{6}$$

In the following, we return to the example of a spin $I = \frac{3}{2}$ to illustrate some concepts of adiabatic passage for a quadrupolar nucleus. We first focus on the evolution of the average spin projection $\langle I_z(t)\rangle = Tr[I_z\rho(t)]$ as we proceed with a linear sweep from $\Delta\nu(t=0) = -\nu_0$ to $\Delta\nu(t=\tau) = +\nu_0$. Fig. S8 shows the result for four different initial conditions corresponding to the pure states of the system. In (a), the adiabatic conditions are fulfilled for the first QTs only. This is evidenced by the exchange of population at the transitions associated with the central peak ($\Delta\nu = 0$) and its two satellites ($\Delta\nu = \pm\nu_Q$). On the contrary, nothing happens at the second QTs ($\Delta\nu = \pm\frac{\nu_Q}{2}$). In (b), the "opening" of the second QTs is evidenced by two additional steps at $\Delta\nu = \pm\frac{\nu_Q}{2}$. As a consequence of the smaller coupling strength, these transitions are sharper compared to the ones observed for the first QTs.

In the next step we retain only the polarization $\langle I_z(\tau)\rangle$ after the sweep is complete and study the effect of a decreasing sweep rate. We first focus on the same set of initial conditions as in Fig. S9. At high sweep rates (here, $\alpha \geq 10^5$ GHz/s) the passage is sudden, $P_{LZ} \simeq 1$, and the polarization remains unchanged after the sweep. For lower values of α, the polarization is modified by the RF pulse. We identify the three thresholds corresponding to fulfilling the adiabatic conditions for the first, second and third QT, respectively. In Fig. S9b, we turn to a more realistic thermal distribution at $t = 0$. The evolution of $\langle I_z(\tau)\rangle$ shows a step-like behaviour, with the steps corresponding to the $\Delta m = 1$, $\Delta m = 2$ and $\Delta m = 3$ thresholds.

Several comments should be made. First, if $\frac{\upsilon_{RF}}{\upsilon_Q} \sim 1$, the different transitions identified in Figs. S7 and S8 are no longer isolated one from the other, and the step-like behaviour of Fig. S9 vanishes. Second, the efficiency of the manipulation for a given sweep rate is not only related the quadrupole field but also to the initial polarization. To clarify this point, let us consider an initial thermal distribution described by a temperature T. In the high temperature limit ($k_BT \gg h\nu_L$, with $h\nu_L$ the Zeeman energy), it is possible to show analytically that the manipulation efficiencies associated with the successive opening of the first,

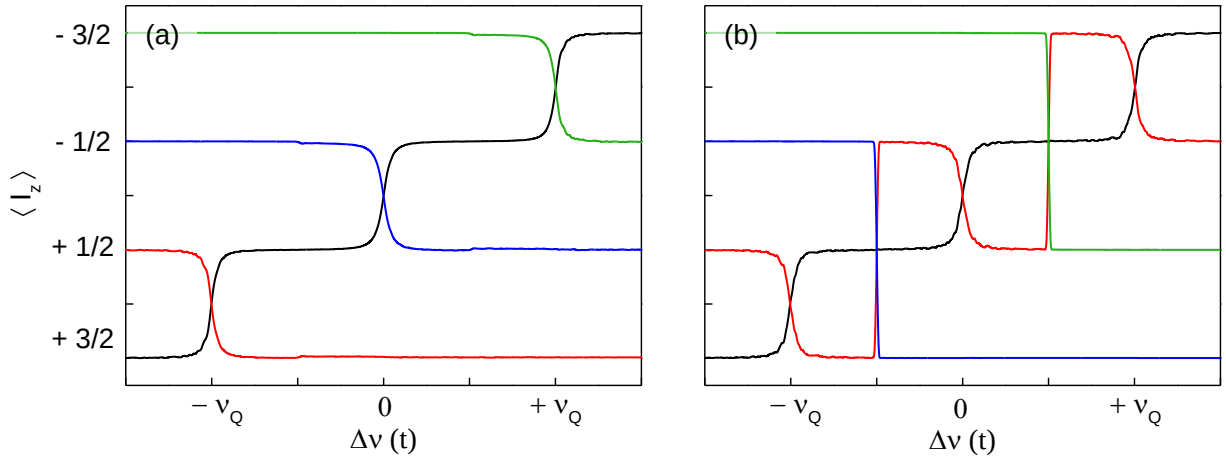

FIG. S8. **Evolution of the average nuclear spin projection $\langle I_z \rangle$ for a linear RF sweep**. The RF field is swept from negative to positive detunings (left to right). In (a), $P_{LZ}(\Delta m = 1) = 1.4\,\%$ and $P_{LZ}(\Delta m = 2) = P_{LZ}(\Delta m = 3) = 100\%$. In (b), $P_{LZ}(\Delta m = 1) = 0$, $P_{LZ}(\Delta m = 2) = 0.5\%$ and $P_{LZ}(\Delta m = 3) = 99.8\%$. For both cases four different initial conditions are considered, corresponding to the pure states of the system. Black: $|\psi(t=0)\rangle = |+\frac{3}{2}\rangle$, red: $|\psi(t=0)\rangle = |+\frac{1}{2}\rangle$, blue: $|\psi(t=0)\rangle = |-\frac{1}{2}\rangle$ and green: $|\psi(t=0)\rangle = |-\frac{3}{2}\rangle$

.

second and third QTs are 60%, 90%, and 100%, respectively. Conversely, in the limit where $k_B T \ll h\nu_L$, complete inversion is achieved as soon as the adiabatic condition is satisfied for the first QT, which does not (to first order) depend on ν_Q.

B. Quantitative analysis

The nuclear spin ensemble in an $In_xGa_{1-x}As$ QD is highly inhomogeneous. The first obvious reason is the presence of various isotopes, mainly ^{75}As, ^{115}In, ^{69}Ga and ^{71}Ga (see Table II). A second reason, which is intrinsic to self-assembled QDs, is the strain which is not homogenously distributed over the QD [10]. This results in a position dependent electric-field gradient, and thus a distribution of quadrupole frequencies over the spin ensemble. This inhomogeneity, associated with the exact chemical composition of the QD, influences the overall degree of adiabaticity that can be reached for a given experiment. In the following we derive the effective nuclear spin temperature following optical polarization, a quantitative value for the chemical composition, as well as the isotope dependent quadrupole frequency distribution in the QD.

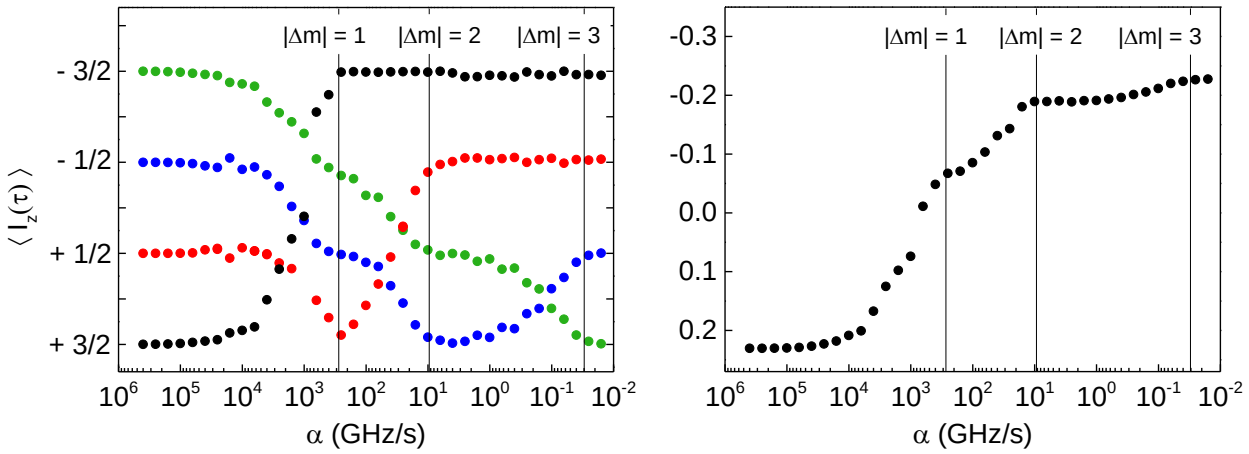

FIG. S9. **Average spin projection $\langle I_z \rangle$ as a function of the sweep rate.** The simulations are carried out on ^{71}Ga with $B_z = 6\,$T, $B_x = 16\,$mT and $\nu_Q = 1\,$MHz for different initial polarizations. In (a), we consider the same pure states as in Fig. S8. For $\alpha \geq 10^5\,$GHz/s the passage is sudden. After the first threshold, the adiabatic condition is satisfied for the first QTs ($|\Delta m| = 1$). We observe, for example, $|+\frac{3}{2}\rangle \rightarrow |-\frac{3}{2}\rangle$ and $|-\frac{3}{2}\rangle \rightarrow |+-\frac{1}{2}\rangle$ as expected from the energy level diagram in Fig. S7. After the second (third) threshold, the adiabatic condition is also satisfied for $|\Delta m| = 2$ ($|\Delta m| = 3$). This has no impact if the population was initially all in the $|+\frac{3}{2}\rangle$ state (black line), but now $|-\frac{3}{2}\rangle \rightarrow |+\frac{1}{2}\rangle$ $\big(|-\frac{3}{2}\rangle \rightarrow |+\frac{3}{2}\rangle$, green line$\big)$. In (b) we start with a thermal distribution with $T = 20\,$mK. The vertical lines correspond to $P_{LZ} = 1\%$ for the first, second and third quantum transitions.

	I	C [%]	γ [MHz/T]	A[μeV]	Q [mb]
^{69}Ga	3/2	60.18	10.219	74	171
^{71}Ga	3/2	39.89	12.984	96	107
^{75}As	3/2	100	7.219	86	314
^{113}In	9/2	4.29	9.310	110	759
^{115}In	9/2	95.71	9.330	110	770

TABLE II. **Relevant parameters of the QD main isotopes:** Nuclear spin number I, natural abundance C, gyromagnetic ratio γ, contact hyperfine coupling strength A and quadrupole moments Q for the relevant isotopes. Since ^{113}In abundance is only 4.3% and its difference in γ compared to ^{115}In is beyond the resolution of our experiment we neglect this isotope in our analysis. Data taken from [11].

B1. Chemical composition and nuclear spin temperature

Since the orbital part of the hole wave function is predominantly p-like, the contact interaction of the nuclear spin ensemble with the hole spin can be neglected. Initialization and read-out thus depends primarily on the contact hyperfine interaction between the nuclear spin ensemble and the electron spin. The effect

of the nuclear spin ensemble on the electron spin is described by an effective magnetic field B_N, the Overhauser field, which shifts the energy levels of the electron spin states. This Overhauser shift is given by OHS $= g_e \mu_B B_N S_z$, where g_e is the effective electron g-factor, μ_B the Bohr magneton and S_z the electron spin quantum number along the z-direction. For a spin ensemble of isotope j with average polarization $\langle I_{z,j} \rangle$, $\mathrm{OHS} = \sum_j A \langle I_{z,j} \rangle S_z$, where A is the hyperfine coupling constant[11, 12]. The experiments presented in the main article are all carried out on the blue transition such that $S_z = -\frac{1}{2}$. Each nuclear spin interacts with the same pumped electron spin so that it is safe to assume that the initial populations of the nuclear spin levels for each isotope can be described with a temperature. It is not necessarily the case that each isotope can be described with the same temperature. For simplicity, we describe all isotopes with the same nuclear spin temperature and we return to this assumption in Section IIID. We now show that measurements of OHS, the initial Overhauser shift, and $\Delta_{\mathrm{OHS}}(\Delta m = 1)$, the change in Overhauser shift measured at the first plateau (Fig. 3 of the main paper), we can determine the In composition x and the initial nuclear spin temperature T.

Using Boltzmann statistics the occupation probability of the m^{th} level for isotope j is

$$p_{j,m} = \frac{1}{Z_j} \exp\left(-\frac{E_{j,m}}{k_B T}\right) \tag{7}$$

where $E_{j,m} = -mh\gamma_j B_z$ is the Zeeman energy of the m^{th} level [13] , $Z_j = \sum_m \exp(-E_{j,m}/kT)$ is the partition function, k_B is the Boltzmann constant and $m = \frac{3}{2}, \frac{1}{2}, -\frac{1}{2}, -\frac{3}{2}$ for $I = \frac{3}{2}$ spins ($m = \frac{9}{2}, \frac{7}{2}, ..., -\frac{9}{2}$, for $I = \frac{9}{2}$ spins). Thus the average nuclear spin polarization for j^{th} isotope amounts to

$$\langle I_{z,j} \rangle = \sum_m p_{j,m} m. \tag{8}$$

By weighting each $\langle I_{z,j} \rangle$ with its corresponding coupling coefficient A_j (see Table II) and relative concentration c_j the initial Overhauser shift for each isotope is

$$\mathrm{OHS}_j = -\frac{1}{2} c_j A_j \langle I_{z,j}^{initial} \rangle. \tag{9}$$

Since Ga substitutes to In, the ^{75}As concentration is known and equals to 50%, whereas the other concentrations depends on x.

An adiabatic sweep leads to a change in nuclear spin polarization

$$\Delta I_{z,j} = \langle I_{z,j}^{final} \rangle - \langle I_{z,j}^{initial} \rangle. \tag{10}$$

Thus the related change in Overhauser shift is

$$\Delta_{\mathrm{OHS}}^{j} = \frac{1}{2} c_j A_j \Delta I_{z,j}. \tag{11}$$

For $\frac{3}{2}$-spins, assuming adiabatic conditions for the first order QTs only, one can determine the final nuclear spin polarization (see energy level diagram of Fig. S7):

$$\langle I_{z,j}^{final}\rangle(\Delta m=1) = +\frac{3}{2}p_{j,\frac{1}{2}} + \frac{1}{2}p_{j,-\frac{1}{2}} - \frac{1}{2}p_{j,-\frac{3}{2}} - \frac{3}{2}p_{j,\frac{3}{2}} \tag{12}$$

The same is done analogously for the $\frac{9}{2}$-spins of indium.

We are finally left with the following set of equations

$$\mathrm{OHS} = \sum_j \mathrm{OHS_j} \tag{13}$$

$$\Delta_{\mathrm{OHS}}(\Delta m=1) = \sum_j \Delta^j_{\mathrm{OHS}}(\Delta m=1) \tag{14}$$

where T and x as the only unknowns. Solving the system with inputs from the experiment $\mathrm{OHS} = (27.0 \pm 0.85)$ μeV and $\Delta_{\mathrm{OHS}} = (28.8 \pm 0.85)$ μeV, we obtain an initial temperature $T = 8.2 \pm 0.8$ mK and an In concentration for this specific QD of $x = 0.202 \pm 0.057$.

B2. Quadrupolar field

In section A, we showed how we use the von Neumann equation to simulate the evolution of the (projected) nuclear spin polarization with a linear sweep of the radio-frequency. Now assuming an initial spin temperature of 8.2 mK, we are in a position to model the NMR spectra measured in our experiment.

We first plot the expected change of polarization in the case of a single ^{71}Ga spin for different quadrupole frequencies, Fig. S10. The simulations show clear steps associated with the transfer of population at the first and second quantum transitions. As expected, the total $\langle \Delta I_z \rangle$ reduces as ν_Q increases, a consequence of the smaller ν_{eff} for the high order QTs. In order to account for the inhomogeneity in the sample, we then average this behaviour over a distribution of quadrupole frequency ($\nu_Q = 0 \rightarrow \nu_Q^{max}$) using (truncated) Gaussian distributions of the form

$$p(\nu_Q) = \lambda \exp\left[\frac{(\nu_Q - \nu_Q^0)^2}{2\sigma_Q^2}\right] \qquad \text{with } \nu_Q > 0, \tag{15}$$

where λ normalizes the distribution, $\int_0^{\nu_Q^{max}} p(\nu_Q) d\nu_Q = 1$. The result is shown in Fig. S10b. We note in particular that the steps associated with the satellite peaks are smeared out as the distribution spreads. Ultimately, the NMR spectrum of the $\frac{3}{2}$-spin reduces to one step at the position of the central frequency surrounded by a steady (almost linear) increase due to the satellite transitions.

For In, the situation is similar, Fig. S11b. After the averaging however, no step remains, a consequence of the large number of transitions.

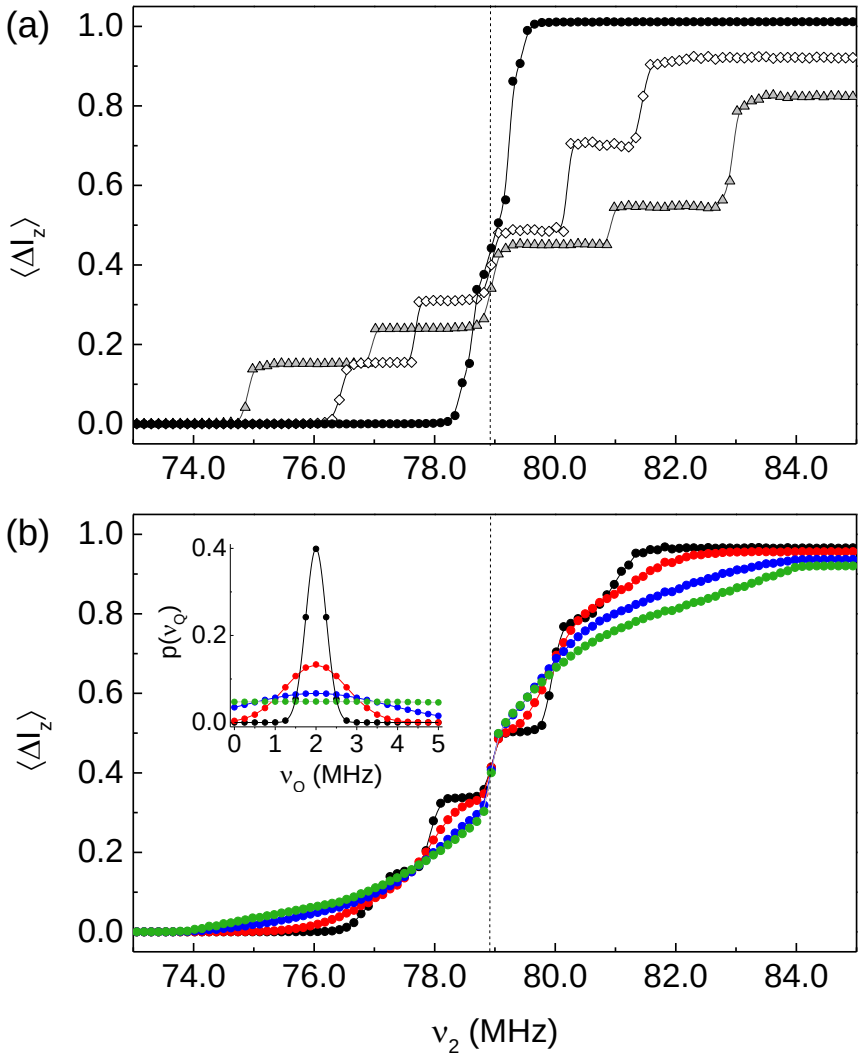

FIG. S10. **NMR spectrum of $\frac{3}{2}$-spins.** (a) Change in polarization for a single ^{71}Ga spin. The sweep rate is set to $\alpha = 0.04\,\mathrm{GHz/s}$ (first and second QTs opened). Three different quadrupole frequencies are shown: black circles $\nu_Q = 0.5\,\mathrm{MHz}$, open diamonds $\nu_Q = 2.5\,\mathrm{MHz}$ and gray triangles $\nu_Q = 4.5\,\mathrm{MHz}$. (b) Change in polarization for an inhomogeneous ensemble of ^{71}Ga spins. In black, red and blue, the distribution of quadrupole frequencies are Gaussian functions centered around $\nu_Q^0 = 2\,\mathrm{MHz}$. In green we consider a flat distribution. Insets: the quadrupole frequency distributions. For all calculations, $B_z = 6\,\mathrm{T}$, $B_x = 3.8\,\mathrm{mT}$ and the initial temperature is set to $T = 8.2\,\mathrm{mK}$.

We finally compute an average quadrupole frequency $\langle \nu_Q \rangle = \int_0^{\nu_Q^{max}} p(\nu_Q)\nu_Q d\nu_Q$, which slightly differs from ν_Q^0 if $p(\nu_Q)$ is truncated.

In order to describe the experimental data, we derive such spectra using the experimental sweep rate $\alpha = 0.09\,\mathrm{GHz/s}$ for $\frac{3}{2}$-spins, and a slightly larger value $\alpha = 0.25\,\mathrm{GHz/s}$ for $\frac{9}{2}$-spins [14]. Weighting each isotope's contribution with its concentration determined in section B 1, and multiplying by the corresponding coupling coefficient (see Table II), we obtain the theoretical spectra shown in Fig. 4 of the main paper. In

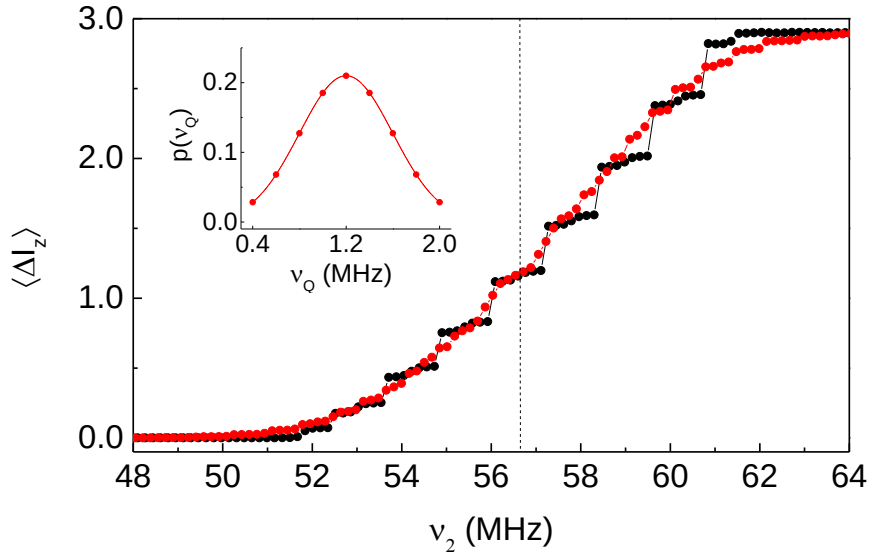

FIG. S11. **NMR spectrum of $\frac{9}{2}$-spins.** Change in polarization for In, with $\alpha = 1\,\text{GHz/s}$. In black, the signal associated with a single spin with $\nu_Q = 1.2\,\text{MHz}$; in red, an inhomogeneous ensemble with a Gaussian distribution of quadrupole frequencies centred around $\nu_Q^0 = 1.2\,\text{MHz}$ (see inset).

the case of ^{75}As and ^{71}Ga, the resonances are well isolated and it is straightforward to adjust $p(\nu_Q)$ to fit the data. On the other hand, for ^{115}In and ^{69}Ga, the spectra overlap. Assuming a homogeneous distribution of both Ga isotopes within the QD (and thus similar electric field gradient distributions), we can however predict the ^{69}Ga spectrum simply by the ratio of both isotope's nuclear quadrupole moments using Eq. 3 (see also Table II). The remaining signal is then due to In. With this procedure we can thus determine an approximate distribution of quadrupole frequencies for all the main isotopes, see Table III and inset of Fig 4.

	^{75}As	^{115}In	^{69}Ga	^{71}Ga
ν_Q^0 [MHz]	0	1.5	2.9	1.8
σ_Q [MHz]	4.0	0.4	1.6	1.6
$\langle\nu_Q\rangle$ [MHz]	3.0	1.5	3.1	2.1

TABLE III. Parameters of the (truncated) Gaussian distributions used in the description of the experimental data, Fig. 3 of the main paper. ν_Q^0 is the central frequency, corresponding to the highest density, σ_Q is the width of the distribution and $\langle\nu_Q\rangle$ is the average quadrupole frequency, which differs from ν_Q^0 when the distribution is truncated.

C. Discussion and conclusions

Now using the temperature and In concentration determined in section B1, with the average quadrupole frequencies for each isotopes determined in section B2 , we can simulate the expected change in the average nuclear spin polarization as a function α (data of Fig. 3 in the main paper). With $B_x = 3.8\,\mathrm{mT}$, the calculations show remarkable agreement with the experimental data. In particular the plateau associated with the first QTs is reproduced, a signature of a large quadrupole field for all isotopes. One can note that the first QTs are not reached at the same α for all isotopes. This is due to different gyromagnetic ratios (see Table II) and, in the case of In, to the different spin number. As can be seen from the isotope selective α-dependency, the second step-like feature at low α arises due to In spins reaching the plateau associated with the second QTs before the $\frac{3}{2}$-spins. The large contribution of the In spins along with the small dispersion in In quadrupole frequencies explain the observed second step-like feature.

Finally, we gather all the results obtained from our calculations and compare them with the experimental data. The results are shown in Fig. S12 and Table IV and commented hereafter:

Initial polarization: The initial polarization for each isotope $\langle I_{z,j}\rangle / I_{z,j}^{max}$ is determined solely by T. Due to the different gyromagnetic ratios and the much higher spin number of In, the polarization is not equally distributed among the different isotopes (Table IV). For example, the initial polarization of As is only 21%, whereas the initial polarization of In reaches 50%. Weighting each isotope with its concentration yields a value of 32% for the initial polarization of the ensemble. Finally, using the coupling coefficients A_j from Table II and our measured value $g_e = -0.71 \pm 0.05$ of the electron g-factor, we calculate the Overhauser field corresponding to 32% polarization, $B_N = 2.0\,\mathrm{T}$.

Efficiency of the nuclear spin manipulation: The inversion efficiency for each isotope is defined as $\Delta I_{z,j}/(2I_{z,j}^{initial}) = \Delta_{\mathrm{OHS}}^{j}/(2\mathrm{OHS_j})$. The efficiency depends on three parameters, first the spin quantum number I, second the initial polarization, and third the quadrupole frequency. ^{75}As has the lowest initial polarization, a broad quadrupole frequency distribution and a large $\langle\nu_Q\rangle$, thus the inversion efficiency (75%) is lower than that for ^{71}Ga (94%), which has a higher initial polarization and a smaller $\langle\nu_Q\rangle$ with a narrower distribution. Conversely, In has a much more complex level structure and despite the high initial polarization the inversion efficiency is only 64%. By weighting the efficiency for each isotope with its concentration we compute the efficiency for the whole ensemble, which is 72%.

Sensitivity of the measurement: The sensitivity to the change in Overhauser shift is obtained from the statistical distribution of the experimental results. Averaging over more than 20 measurements, we obtain a standard deviation of 0.85 μeV for Δ_{OHS}. Using the value $\mathrm{OHS}^{\mathrm{max}} = 81.8\,\mu\mathrm{eV}$ for the maximum Over-

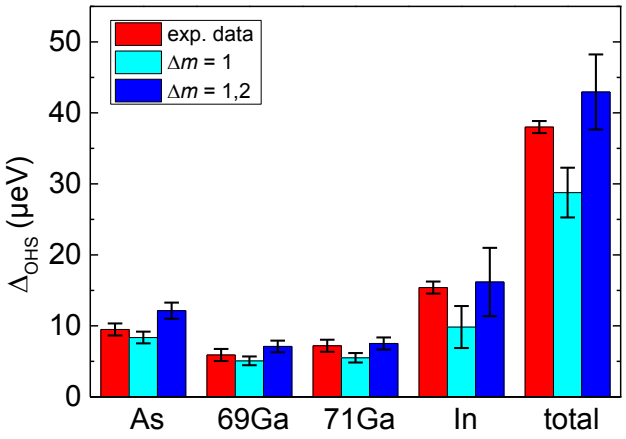

FIG. S12. **Comparison of the measured change in Overhauser shift Δ_{OHS} with the single spin model at first and second quantum transitions.** The results indicate that, for the slowest rate, we achieve inversion at the second QT for In and ^{71}Ga. The second QT is however not yet opened for As and ^{69}Ga. Input parameters to the model are $T = 8.2 \pm 0.8$ mK and $x = 0.20 \pm 0.06$.

hauser shift and 10^5 nuclei [12], we conclude that we are sensitive to the Overhauser field generated by the full polarization of $\sim 1,000$ nuclei. The errors in x and T correspond to the statistical fluctuations in the change of the plateau width. For all numbers deduced from the model the errors in the change of dragging plateau width were propagated to find the error in a particular quantity.

-	^{75}As	^{69}Ga	^{71}Ga	^{115}In	total
OHS [μeV]	-6.6 ± 0.6	-3.80 ± 0.4	-4.0 ± 0.4	-12.6 ± 3.6	-27.0 ± 0.9
Initial Polarization [%]	21 ± 3	29 ± 3	36 ± 3	50 ± 3	32 ± 1
$\Delta_{\mathrm{OHS}}(\Delta m = 1)$ [μeV]	8.4 ± 0.8	5.1 ± 0.6	5.5 ± 0.7	9.8 ± 4.8	28.8 ± 0.9
Inversion efficiency ($\Delta m = 1$) [%]	63.0 ± 0.5	66.3 ± 0.7	68.8 ± 0.9	39.2 ± 1.3	55.0 ± 2.3
$\Delta_{\mathrm{OHS}}(\Delta m = 1,2)$ [μeV]	12.1 ± 1.1	7.1 ± 0.8	7.5 ± 0.9	16.2 ± 4.8	42.9 ± 5.3
Inversion efficiency ($\Delta m = 1,2$) [%]	91.6 ± 0.2	92.9 ± 0.3	93.9 ± 0.3	64.5 ± 1.5	81.3 ± 2.4
Δ_{OHS}(measured) [μeV]	9.5 ± 0.9	5.9 ± 0.9	7.2 ± 0.9	15.4 ± 0.9	38 ± 0.9
Inversion efficiency (measured) [%]	75 ± 9	71 ± 14	94 ± 15	64 ± 19	72 ± 10

TABLE IV. **Initial polarizations and manipulation efficiencies for the main isotopes**. Values in red are obtained from Figs. 2, 3 and 4. Values in black are deduced from the single spin model described in Section *B1* with $T = 8.2$ mK and $x = 20\%$.

D. Nuclear spin temperature

The analysis so far has assumed an isotope-independent initial nuclear spin temperature. An alternative assumption is that the polarization for all spin-$\frac{3}{2}$ nuclei is the same such that there is a spread of temperatures in accord with the spread in gyromagnetic ratios. This second Ansatz would hold if the only significant interaction is the first-order contact hyperfine interaction [15]. We have attempted to describe the experimental data also with this assumption, explicitly that the ratio $\beta = (E_{j,m+1} - E_{j,m})/k_B T$ (ratio Zeeman energy to thermal energy) is the same for all isotopes. We find with this approach that $\beta = 0.302 \pm 0.033$, $x = 0.221 \pm 0.067$ with temperatures ^{75}As: (6.9 ± 0.8) mK; In: (8.9 ± 1.0) mK; ^{69}Ga: (9.7 ± 1.1) mK; ^{71}Ga: (12.4 ± 1.4) mK. Some important comments are in order.

First, the indium concentration from the common polarization assumption is the same to within the random error as before (common temperature assumption). The random error is determined by noise in the initialization/read-out process. In other words, the random error is larger than any systematic error arising from assumptions on the temperature.

Secondly, the temperatures for ^{75}As, In and ^{69}Ga are also the same as before to within the random error: the common temperature and common polarization assumptions do not lead to significant differences. In principle, the experiment is capable of determining a nuclear spin temperature for each isotope separately. In practice, the present resolution is insufficient to reveal small differences.

Thirdly, the two assumptions, common temperature versus common polarization, lead to significantly different temperatures for ^{71}Ga. A detailed comparison of the two models is shown in Fig. S13 which plots Δ_{OHS}, measured and calculated. The ^{71}Ga result from the common polarization model is significantly too small, and this discrepancy cannot be resolved by including full inversion at the second quantum transition or by reducing the In concentration. The conclusion is that the common temperature assumption is more realistic than the common polarization assumption. This points to the presence of another interaction in the initialization process. A likely explanation is that the electron spin in the exciton provides a mechanism by which all the nuclear spins are coupled together, a second-order process, in the presence of spontaneous emission of the exciton which blurs energy conservation of the electron-nuclear interactions by up to 1 μeV.

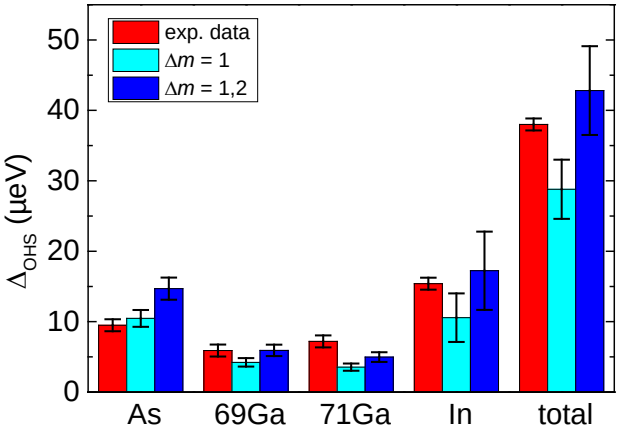

FIG. S13. **Comparison of the measured change in Overhauser shift Δ_{OHS} with the single spin model at first and second quantum transitions with the common polarization assumption.** As in Fig. S12, for the slowest rate we achieve inversion at the first and second QT for In and ^{71}Ga but inversion at the first QT only for As and ^{69}Ga. Input parameters to the model are $\beta = 0.302$ and $x = 0.221$. The calculations for ^{71}Ga lie below the experimental result and in this respect, the common polarization assumption is inferior to the common temperature assumption of Fig. S12.

[1] Kuhlmann, A. V. *et al.* A dark-field microscope for background-free detection of resonance fluorescence from single semiconductor quantum dots operating in a set-and-forget mode. *Review of Scientific Instruments* **84**, 073905 (2013).

[2] Latta, C. *et al.* Confluence of resonant laser excitation and bidirectional quantum-dot nuclear-spin polarization. *Nature Physics* **5**, 758–763 (2009).

[3] Högele, A. *et al.* Dynamic nuclear spin polarization in the resonant laser excitation of an ingaas quantum dot. *Phys. Rev. Lett.* **108**, 197403 (2012).

[4] Maletinsky, P., Badolato, A. & Imamoglu, A. Dynamics of quantum dot nuclear spin polarization controlled by a single electron. *Phys. Rev. Lett.* **99**, 056804 (2007).

[5] Poggio, M., Degen, C. L., Rettner, C., Mamin, H. & Rugar, D. Nuclear magnetic resonance force microscopy with a microwire rf source. *Applied Physics Letters* **90**, 263111 (2007).

[6] Harris, R. & Roderick, W. (eds.) *NMR of Quadrupolar Nuclei in Solid Materials* (Wiley, 2012).

[7] Vega, S. Fictitious spin 1/2 operator formalism for multiple quantum NMR. *The Journal of Chemical Physics* **68**, 5518–5527 (1978).

[8] van Veenendaal, E., Meier, B. H. & Kentgens, A. P. M. Frequency stepped adiabatic passage excitation of half-integer quadrupolar spin systems. *Molecular Physics* **93**, 195–213 (1998).

[9] Haase, J., Conradi, M., Grey, C. & Vega, A. Population transfers for NMR of quadrupolar spins in solids. *Journal of Magnetic Resonance, Series A* **109**, 90–97 (1994).

[10] Bulutay, C. Quadrupolar spectra of nuclear spins in strained ingaas quantum dots. *Phys. Rev. B* **85**, 115313 (2012).

[11] Coish, W. A. & Baugh, J. Nuclear spins in nanostructures. *physica status solidi (b)* **246**, 2203–2215 (2009).

[12] Kloeffel, C. *et al.* Controlling the interaction of electron and nuclear spins in a tunnel-coupled quantum dot. *Phys. Rev. Lett.* **106**, 046802 (2011).

[13] Corrections to the level spacings due to first order quadrupolar effects (Eq. 1) were included in a mean approach by using the average quadrupole frequency determined in section B.2 for each isotope. Note that, given $\langle \nu_Q \rangle \ll \gamma B_z$, the effect on T and x are small and fall within the error bars.

[14] By doing so we significantly speed up calculations without modifying the expected result since both rates belong to the second plateau for In, see Fig. 3.

[15] Abragam, A. *Principles of Nuclear Magnetism* (Oxford University Press, 2002).